TU Delft

Delft University of Technology

Document Version
Final published version

Licence
CC BY

Citation (APA)
Qu, B., Ding, J., Chen, Y., Huang, C., Zhou, R., Wang, L., & Hintzen, H. T. (2026). Luminescence manipulation of Cu-doped $CaAl_2O_4$ phosphors via selective Cu^{+}/Cu^{2+} valence state regulation. *Journal of Materials Chemistry C*. https://doi.org/10.1039/d6tc01463a

Important note
To cite this publication, please use the final published version (if applicable).
Please check the document version above.

Copyright
In case the licence states “Dutch Copyright Act (Article 25fa)”, this publication was made available Green Open Access via the TU Delft Institutional Repository pursuant to Dutch Copyright Act (Article 25fa, the Taverne amendment). This provision does not affect copyright ownership.
Unless copyright is transferred by contract or statute, it remains with the copyright holder.

Sharing and reuse
Other than for strictly personal use, it is not permitted to download, forward or distribute the text or part of it, without the consent of the author(s) and/or copyright holder(s), unless the work is under an open content license such as Creative Commons.

Takedown policy
Please contact us and provide details if you believe this document breaches copyrights.
We will remove access to the work immediately and investigate your claim.

This work is downloaded from Delft University of Technology.

Journal of Materials Chemistry C

ROYAL SOCIETY OF CHEMISTRY

PAPER

Published on 01 July 2026
Licence and permissions

Check for updates

Cite this: DOI: 10.1039/d6tc01463a

Luminescence manipulation of Cu-doped $CaAl_2O_4$ phosphors *via* selective Cu^+/Cu^{2+} valence state regulation

Bingyan Qu,[a] Junxiang Ding,[a] Yang Chen,[a] Chenglan Huang,[a] Rulong Zhou,[a] Lei Wang *[ac] and Hubertus T. Hintzen*[b]

Received 7th May 2026,
Accepted 30th June 2026

DOI: 10.1039/d6tc01463a

rsc.li/materials-c

Copper ions (Cu^+ and Cu^{2+}) serve as important luminescent centers in various inorganic materials but often coexist within the same host lattice. Both ions exhibit broadband emissions with analogous peak shapes and closely overlapping peak positions. This spectral similarity, however, makes it extremely challenging to distinguish Cu^+ and Cu^{2+} from each other *via* conventional luminescence spectroscopy, which hinders in-depth investigations into their distinct luminescent mechanisms and limits the exploration of their application potential in advanced optical systems. In this work, we address this challenge by actively manipulating the valence states of Cu ions doped in $CaAl_2O_4$ through selective co-doping with mono-valent Na^+ and trivalent lanthanide ions ($La^{3+}/Tb^{3+}/Dy^{3+}$). Combined experimental and first-principles studies reveal that Na^+ doping effectively stabilizes Cu^{2+}, leading to an intense blue emission centered at 471 nm. Conversely, co-doping with trivalent lanthanides promotes the formation of Cu^+, resulting in a bright green emission peak at 501 nm. Leveraging this valence tunability, we demonstrate a prototype optical encoding device based on their cooperative luminescence, highlighting its promising utility in anti-counterfeiting technologies. This study not only provides a fundamental understanding for deciphering and controlling the luminescence of copper ions with different valencies, but also offers valuable guidance for the design of novel multifunctional Cu-activated phosphors.

1. Introduction

Copper ions (Cu^+/Cu^{2+}) are pivotal activator centers in inorganic phosphors, exhibiting distinct valence-dependent luminescent behaviors that provide versatile design opportunities for high-performance optical materials.[1–3] Specifically, Cu^{2+} ions with a $3d^9$ electronic configuration can generate intense, tunable visible emission *via* ligand-to-metal charge transfer (LMCT) processes under specific coordination environments. This effect has been validated in diverse materials, including Cu^{2+}-doped $SrGa_2O_4$[4,5] (red emission), $BaGa_2O_4$[6] (yellow emission), $Ba_{0.4}Sr_{1.6}Ga_4O_8$[7,8] and $SrGa_2Ge_2O_8$[9,10] (green emission), as well as $ZnAl_2O_4$[11] and $BaAl_2O_4$[12] (blue emission). Meanwhile, Cu^+ ions with a closed-shell $3d^{10}$ structure typically produce broadband visible emission *via* 4s → 3d radiative transitions.[13] Examples include Cu^+-doped $SrAl_4O_7$[14] (green emission), Rb_2AgBr_3[15] (blue emission), and Pb(OH)Br[16] (red emission). Such versatile luminescence characteristics render copper-activated materials highly promising for applications in solid-state lighting, display technologies, optical storage, and anti-counterfeiting.

Despite these advantages, a critical bottleneck persists in the study and application of Cu-activated phosphors. During synthesis under a weakly oxidizing atmosphere, Cu ions may be directly reduced to metallic Cu, whereas under a stronger oxidizing atmosphere, a mixture of Cu^+ and Cu^{2+} still tends to form rather than a single valence state. Frequently, both Cu^+ and Cu^{2+} produce broadband emissions with analogous peak shapes and closely overlapping peak positions, as observed in CsBr:Cu,[17] $SrZrO_3$:Cu,[18] and Na_2SO_4:Cu.[19] This spectral overlap makes it extremely challenging to distinguish the two valence states *via* luminescence spectroscopy alone, especially considering that their luminescence lifetimes are also similar. Compounding this issue, the overlapping X-ray photoelectron spectroscopy (XPS) signals of Cu^+ and Cu^{2+}[20,21] coupled with the electron paramagnetic resonance (EPR) silence of Cu^+[22] prevent accurate quantitative characterization of their relative

[a] School of Materials Science and Engineering, Hefei University of Technology, Hefei, 230009, Anhui, China. E-mail: leiwang@hfut.edu.cn
[b] Fundamental Aspects of Materials and Energy, Delft University of Technology, Mekelweg 15, Delft, 2629 JB, Netherlands. E-mail: H.T.Hintzen@tudelft.nl
[c] Engineering Research Center of High Performance Copper Alloy Materials and Processing, Ministry of Education, Hefei University of Technology, Hefei, 230009, China

concentrations using conventional analytical techniques. These limitations not only hinder the identification of Cu^{+}/Cu^{2+}-specific luminescent behaviors but also impede in-depth investigations into their intrinsic luminescence regularity and underlying mechanisms. Thus, developing effective strategies to differentiate the valence states of Cu ions and establish their corresponding luminescent behaviors is essentially important.

On the other hand, the mixed-valence coexistence of Cu^{+}/Cu^{2+} in a single host enables excitation-dependent dual emission. This emission can be tailored to tunable optical outputs.[23,24] This feature aligns with the demand for advanced information security technologies, particularly in the field of next-generation optical information encryption.[25–27] Compared with traditional strategies such as co-doping multiple luminescent centers,[28,29] utilizing a single multivalent activator (*e.g.*, Cu ions) to realize diversified emission provides a promising pathway. Therefore, the deliberate manipulation of Cu^{+}/Cu^{2+} valence states and thereby control of their relative concentrations remain critical issues from both fundamental and applied perspectives.

Herein, we address the aforementioned challenges by reporting the first realization of tunable dual-mode emission from Cu^{+}/Cu^{2+} ions in $CaAl_2O_4$ host. The key innovation lies in a rational strategy that enables controlled modulation of the Cu^{+}/Cu^{2+} equilibrium. Specifically, we will show that Na^{+} doping stabilizes Cu^{2+} while trivalent lanthanide ($La^{3+}/Tb^{3+}/Dy^{3+}$) codoping promotes Cu^{+} formation, which achieves selective enhancement of distinct emission channels. Furthermore, a proof-of-concept optical encoding unit that demonstrates this valence tunability exhibits potential for applications in information security, particularly in advanced anti-counterfeiting systems leveraging their excitation-wavelength-dependent luminescence outputs. This work not only clarifies the dual-mode luminescence mechanisms of Cu ions in aluminate systems but also establishes a generalizable pathway for the rational design of Cu-activated phosphors with controllable emission properties, advancing the development of high-performance Cu^{2+} or Cu^{+} optical materials.

2. Experimental section

2.1. Phosphor preparation

$CaAl_2O_4$:*x*%Cu (x = 0.25, 0.5, 1, 1.5), $CaAl_2O_4$:*x*%Cu,*y*%Na^{+} (x, y = 0.25, 0.5, 1, 1.5), and $CaAl_2O_4$:1%Cu,*y*%Ln^{3+} (Ln = La, Tb, Dy; y = 0.25, 0.5, 1, 1.5) luminescent materials were synthesized *via* a high-temperature solid-state reaction. Herein, *x*% and *y*% represent the nominal molar percentages relative to Ca^{2+} ions. Starting materials $CaCO_3$ (99.95%), Al_2O_3 (99.99%), CuO (99.9%), Na_2CO_3 (99.99%), La_2O_3 (99.9%), Tb_4O_7 (99.9%), and Dy_2O_3 (99.9%) were employed as raw materials and weighed in stoichiometric proportions. The powders were mixed thoroughly by grinding in an agate mortar for 40 minutes, and then transferred to an alumina crucible. The mixture was heated to 900 °C and held for 2 hours in air; after cooling and regrinding, the pre-calcined product was sintered at 1400 °C for 5 hours with a heating rate of 6 °C min^{-1} in air. The product was cooled naturally to room temperature and ground into powder samples for subsequent characterization.

2.2. Characterization

Phase analysis was performed on a D/MAX2500V X-ray diffractometer (Cu Kα radiation, λ = 1.5406 Å). Data were collected over a 2θ range of 10° to 90° at a scanning speed of 10° min^{-1} with a step size of 0.02° (reduced to 0.01° for detailed refinement). Rietveld crystal structure refinement was conducted using the GSAS 2.0 software. Morphology and elemental composition were investigated using a SIGMA thermal field-emission scanning electron microscope (Zeiss) equipped with an energy-dispersive X-ray spectroscopy (EDS) system, operated at 2 kV and 50 mA. Surface chemical states were analyzed by X-ray photoelectron spectroscopy (XPS) on an ESCALAB 250Xi spectrometer (Thermo Fisher Scientific), with binding energies referenced to the C 1s peak at 284.8 eV. Electron paramagnetic resonance (EPR) measurements were performed at 294 K on a JES-X330 spectrometer. Diffuse reflectance spectra (DRS) were recorded on a CARY 5000 UV-vis-NIR spectrophotometer (Agilent Technologies) from 200 to 800 nm. Photoluminescence (PL) excitation and emission spectra were acquired using a Hitachi F-4600 fluorescence spectrophotometer at a scanning speed of 240 nm min^{-1}. The PL quantum yields (PLQYs) were studied by using an Edinburgh FS5 fluorescence spectrophotometer equipped with an integrated sphere. PersL spectra were collected at various time intervals after excitation with a 254 nm UV lamp (9 W). Temperature-dependent PL measurements were conducted by interfacing the spectrophotometer with an external TAP-02 temperature controller. Persistent luminescence decay curves were recorded using a Zheda Sensing PR305 PersL device after 30 minutes of 254 nm UV excitation, with emission monitored at 471 nm. Thermoluminescence (TL) measurements were performed on a 3D TL dosimeter. Before measurement, the phosphors were irradiated with 254 nm UV light (9 W) for 5 min, and the TL signals were recorded during heating from 303 to 473 K. All luminescence photographs were captured with a Nikon D7500 camera under darkroom conditions.

2.3. First-principles calculations

First-principles calculations within the framework of density functional theory (DFT) were performed using the VASP code to systematically investigate the site preference, electronic structure, and excitation/emission energies of copper ions in the $CaAl_2O_4$ host. The hybrid PBE0 functional was employed to achieve a more accurate description of the electronic properties and optical transitions. A comprehensive description of the computational parameters is provided in the SI.

3. Results and discussion

3.1. Phase characterization, crystal structure, and valence state control mechanisms

The XRD patterns in Fig. 1(a) reveal that the diffraction peaks of both undoped and Cu-doped $CaAl_2O_4$ samples match the standard card (CIF-2002888) for $CaAl_2O_4$. A closer inspection of

 This journal is © The Royal Society of Chemistry 2026

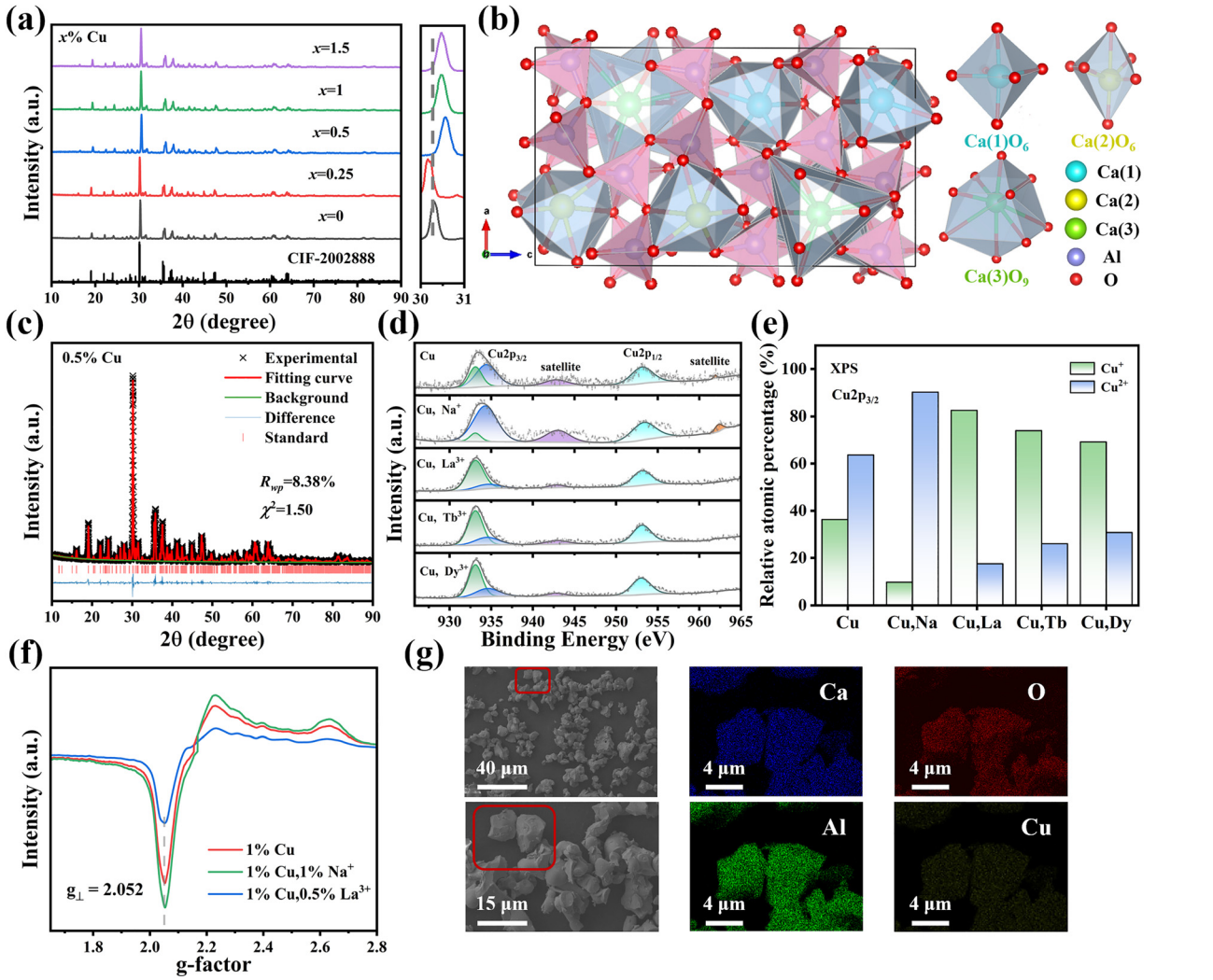


Fig. 1 (a) XRD patterns of $CaAl_2O_4$:x%Cu (x = 0–1.5) and the standard (CIF-2002888) of $CaAl_2O_4$; (b) the schematic crystal structure of $CaAl_2O_4$; (c) Rietveld refinement results of $CaAl_2O_4$:0.5%Cu; (d) Cu 2p XPS spectra of the corresponding sample: $CaAl_2O_4$:1%Cu, $CaAl_2O_4$:1%Cu,1%Na^+, $CaAl_2O_4$:1%Cu,0.5%Ln^{3+}; (e) relative contents of Cu^+ and Cu^{2+} derived from Cu $2p_{3/2}$ peak fitting; (f) EPR spectrum of the corresponding samples: $CaAl_2O_4$:1%Cu, $CaAl_2O_4$:1%Cu,1%Na^+, $CaAl_2O_4$:1%Cu,0.5%La^{3+}. (g) Representative SEM images of the $CaAl_2O_4$:1%Cu sample at different magnifications, alongside the corresponding elemental mapping for Ca, Al, O, and Cu.

the magnified 30–31° region reveals an overall shift of diffraction peaks toward higher angles with increasing Cu concentration. This lattice contraction, together with the ionic radii comparison (Table S1), supports the conclusion that Cu (either Cu^+ or Cu^{2+}) substitutes for the larger Ca^{2+} ions. Fig. 1(c) shows the Rietveld structural refinement performed on the XRD pattern of $CaAl_2O_4$:0.5%Cu. The reliability factors of the refinement are R_{wp} = 8.38% and χ^2 = 1.50. The lattice constants obtained from Rietveld refinement are summarized in Table S2 of the SI. In Fig. 1(b), the crystal structure of $CaAl_2O_4$ belongs to the monoclinic system with space group $P2_1/n$,[30] where Ca^{2+} occupies three non-equivalent sites, namely the six-coordinated irregular octahedra Ca(1) and Ca(2), and the nine-coordinated polyhedron Ca(3).[31,32] To determine the specific site preference among the three inequivalent Ca sites, we calculated the formation energies for Cu^{2+} incorporation, as the low Cu concentration precludes experimental determination by Rietveld refinement. The results indicate that Cu^{2+} is most stable at the Ca(2) site, with a formation energy at least 0.255 eV lower than those of the other two Ca sites, suggesting a thermodynamic preference for occupying this site.

Co-dopants (Na^+, Ln^{3+}) were introduced to modulate the valence state of Cu ions. The XRD patterns of all the samples retain the host crystal structure with no detectable impurity phases (Fig. S1). These findings are further supported by Rietveld refinement results and the convergence of lattice parameters, as summarized in Tables S3 and S4 of the SI. The refined lattice parameters of the Na^+- or Ln^{3+}-*co*-doped samples are nearly identical to those without Na^+ or Ln^{3+}. Given the comparable ionic radii of these dopants to Ca^{2+} (Table S1), it is inferred that they also preferentially occupy Ca^{2+} sites.

In Fig. 1(d), XPS analysis was performed on the $CaAl_2O_4$:1%Cu, $CaAl_2O_4$:1%Cu,1%Na^+, and $CaAl_2O_4$:1%Cu,0.5%Ln^{3+} samples. The spectrum of $CaAl_2O_4$:1%Cu exhibits two intense

main peaks at 933.4 eV and 953.1 eV, corresponding to the Cu $2p_{3/2}$ and $2p_{1/2}$ spin–orbit doublet, a feature common to both Cu^{+} and Cu^{2+} ions due to their closely spaced binding energies.[33] The characteristic satellite peaks located at 942.8 eV and 961.9 eV provide definitive evidence for the presence of Cu^{2+}.[34] Furthermore, the higher-intensity component of the Cu $2p_{3/2}$ doublet at around 933.4 eV was carefully decomposed through peak fitting, resolving two peaks at 933.1 eV (Cu^{+}) and 934.3 eV (Cu^{2+}). Based on the integrated peak areas, a semi-quantitative analysis of the relative Cu^{+} and Cu^{2+} contents was performed (Fig. 1(e)). The enhanced satellite peak intensity, together with the increased relative Cu^{2+} content derived from Cu $2p_{3/2}$ peak fitting, demonstrates that Na^{+} can effectively stabilize a higher proportion of copper ions in the Cu^{2+} oxidation state within the material. This implies that Na^{+} is not incorporated interstitially into $CaAl_2O_4$ (which would stabilize Cu^{+}), but instead largely replaces Ca^{2+} substitutionally, thereby stabilizing the higher valence state of copper (Cu^{2+}). A similar effect has been observed in Na^{+}, Eu^{3+} co-doped $CaAl_2O_4$, where the stability of Eu^{3+} is also enhanced under analogous substitutional incorporation of Na^{+}.[35] In contrast, when Ln^{3+} is added, Cu^{+} becomes the predominant valency of copper in the samples. In addition, the copper Auger lines were examined (Fig. S2). The Auger peaks for Cu^{+} and Cu^{2+} are located at approximately 916.9 eV and 917.8 eV, respectively. Semi-quantitative analysis based on the Auger peak areas yields the same trend as the XPS results, further corroborating the observed manipulation of copper valence states.

The valence state modulation of copper was further corroborated by EPR spectroscopy. The analysis of $CaAl_2O_4$:1%Cu, $CaAl_2O_4$:1%Cu,1%Na^{+}, and $CaAl_2O_4$:1%Cu,0.5%La^{3+} (the latter exhibiting the highest emission intensity among different La-doping levels) revealed a characteristic signal centered at $g_{\perp}$ = 2.052 (Fig. 1(f)), which is a definitive signature of Cu^{2+} with a d^9 electron configuration and unpaired spins.[36] Notably, Cu^{+} (d^{10} configuration, no unpaired spins) is EPR-silent due to its diamagnetic nature. The signal intensity, which is directly proportional to the paramagnetic Cu^{2+} concentration, intensified with Na^{+} incorporation but diminished with La^{3+} doping, in agreement with XPS results. These combined EPR and XPS changes consistently affirm the coexistence of Cu^{+}/Cu^{2+} and the effectiveness of Na^{+} and La^{3+} in modulating the copper valence state in an opposite way.

As shown in Fig. 1(g), the $CaAl_2O_4$:1%Cu sample exhibits irregular polyhedral morphology characterized by densely aggregated particles with a uniform size of approximately 10 μm. This dense, block-like microstructure is a characteristic signature of materials synthesized *via* the high-temperature solid-state reaction method followed by grinding. Moreover, EDS mapping reveals a homogeneous distribution of the constituent elements (Ca, Al, O, and Cu). These results confirm the synthesis of a compositionally uniform $CaAl_2O_4$:Cu luminescent material. The same results were also observed in the Cu–Na^{+}/Dy^{3+} co-doped samples (Fig. S3 and S4).

3.2. Luminescence performance of Cu-doped $CaAl_2O_4$

The optical absorption properties of the undoped and Cu-doped $CaAl_2O_4$ samples were systematically investigated. As illustrated in Fig. 2(a), the undoped host matrix exhibits fundamental absorption bands located below 420 nm. The introduction of Cu ions significantly enhances the absorption intensities across the measured spectrum and gives rise to several distinct absorption bands, centered at approximately 260 nm, 300 nm, 350 nm, and 420 nm. These characteristic absorption features might be attributed to electronic transitions associated with the incorporated copper ions.

In Fig. 2(b), the $CaAl_2O_4$:0.25%Cu sample shows a green emission band centered at 501 nm (FWHM = 55 nm) under excitation. This emission is associated with two broad excitation bands peaking at 344 nm and 399 nm. When the Cu concentration increases to 0.5% (Fig. 2(c)), the intensity of the 501 nm emission decreases. Concurrently, two extra excitation peaks appear at 251 nm and 293 nm. Under excitation at these new wavelengths, a distinct blue emission band centered at 471 nm (FWHM = 95 nm) is observed. With a further increase in Cu concentration (Fig. 2(d) and (e)), their peak positions remain largely unchanged. Notably, the intensity of the 501 nm emission band continues to decrease, whereas the intensity of the 471 nm band increases and reaches its maximum at 1% Cu doping (Fig. 2(f)).

To elucidate the origin of the spectral features in Cu-doped $CaAl_2O_4$, excitation and emission spectra of Na^{+}-codoped samples were collected (Fig. 2(g)). The spectra exhibit excitation peaks at 251 nm and 293 nm, accompanied exclusively by an emission band centered at 471 nm (excited at 293 nm), while the green emission at 501 nm is absent. The position of the emission peak remains at about 471 nm under the excitation of 251 nm (Fig. S5(a)). XPS and EPR analyses confirm that Na^{+} co-doping promotes the stabilization of Cu ions in the +2 oxidation state. Accordingly, the excitation peaks at 251 nm and 293 nm, along with the blue emission at 471 nm, are attributed to Cu^{2+} ions. These luminescence features are assigned to charge-transfer (CT) transitions of Cu^{2+}, consistent with previous reports such as those observed in $SrGa_2O_4$:Cu^{2+} (ref. 4 and 5) and $BaGa_2O_4$:Cu^{2+}.[6] Mechanistically, the CT process entails electron transfer from the O^{2-} 2p orbital to the Cu^{2+} 3d level. Both excitation peaks at 251 and 293 nm correspond to this CT process, and similar dual CT excitation bands of Cu^{2+} have also been observed in systems such as MgO.[37] The subsequent radiative return of the electron to the oxygen center results in the observed blue emission at 471 nm, as depicted schematically in Fig. 2(i).

Based on the assignment above, the excitation peaks at 344 nm and 399 nm, together with the green emission at 501 nm, are attributed to Cu^{+} ions. The excitations at 344 nm and 399 nm arise from electronic transitions from the Cu^{+} 3d orbitals to the split 4s levels. A similar excitation profile has also been reported in spectroscopic studies of Cu^{+}-activated CaS and BaS.[38] To further verify this assignment, La^{3+}-codoped samples were examined (Fig. 2(h)). In these samples, the excitation peaks at 344 nm and 399 nm are observed, along with the characteristic 501 nm emission band excited under 344 nm. Notably, the blue emission at about 471 nm ascribed to Cu^{2+} and its associated excitation bands are absent, confirming that the blue-green emission at 501 nm originates exclusively

 This journal is © The Royal Society of Chemistry 2026

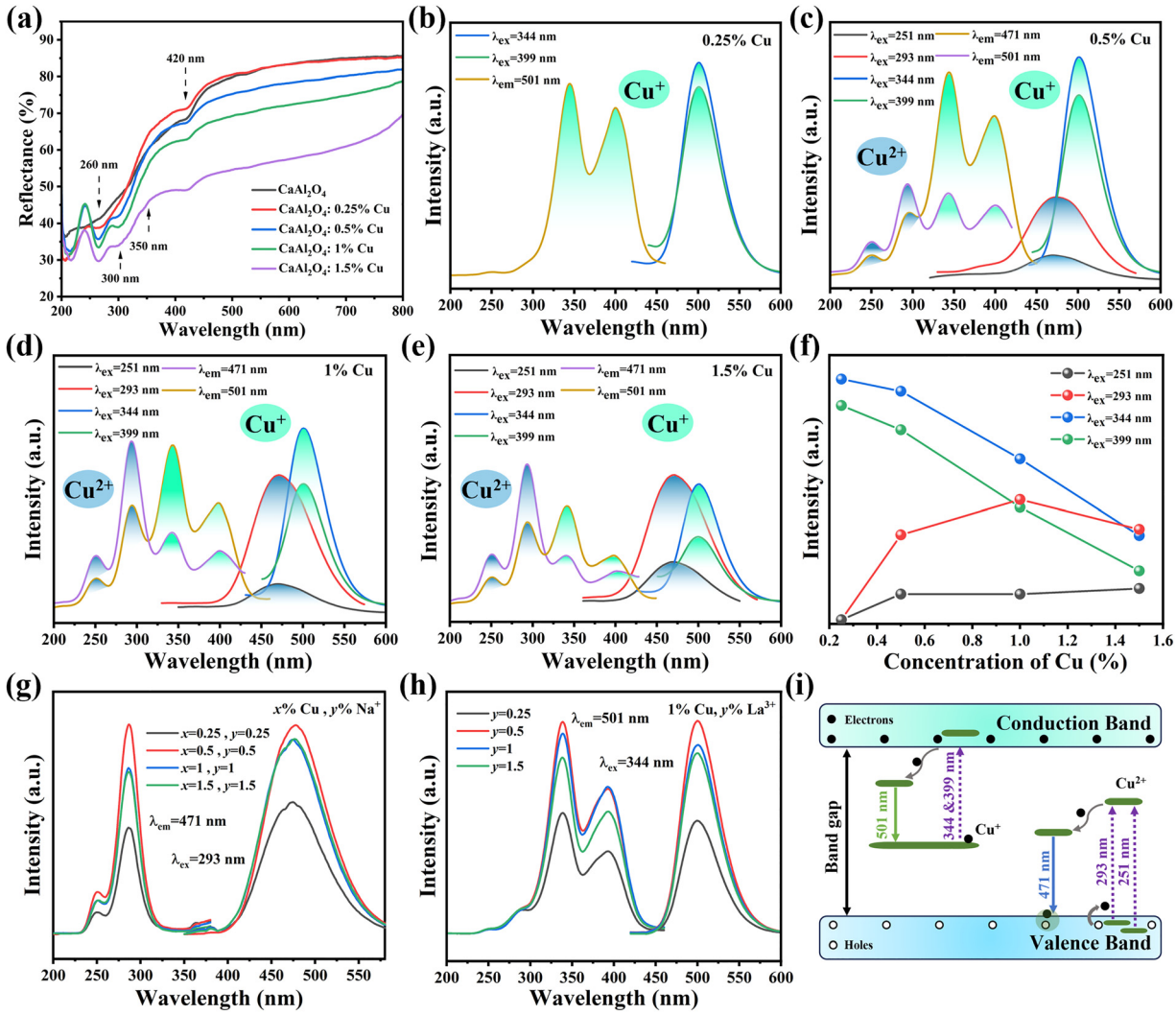


Fig. 2 (a) DRS of $CaAl_2O_4$:*x*%Cu (*x* = 0–1.5), The excitation and emission spectra of $CaAl_2O_4$ with (b) 0.25%Cu, (c) 0.5%Cu, (d) 1%Cu, (e) 1.5%Cu, (g) *x*%Cu,*y*%Na^+ (*x*, *y* = 0.25–1.5), (h) 1%Cu,*y*%La^{3+} (*y* = 0.25–1.5), (f) luminescence intensity with different copper ion concentration, (i) illustration of the luminescence mechanism of $CaAl_2O_4$:Cu^+/Cu^{2+}.

from Cu^+. In addition, the position of the emission peak remains at 501 nm under the excitation of 399 nm (Fig. S5(b)). Supporting conclusions were obtained from additional co-doping experiments with Tb^{3+}/Dy^{3+} and Cu (Fig. S5). Notably, under 344 nm excitation, a small shoulder appears at 540 nm in the PL spectrum of the Tb^{3+} co-doped sample (Fig. S5(c)), superimposed on the Cu^+ emission and assigned to the $^5D_4 \rightarrow {}^7F_5$ characteristic transition of Tb^{3+}[39]; similarly, for the Dy^{3+} co-doped sample (Fig. S5(e)), a shoulder emerges at 570 nm, attributed to the $^4F_{9/2} \rightarrow {}^6H_{13/2}$ transition of Dy^{3+}.[40] The incorporation of La^{3+}, Tb^{3+}, or Dy^{3+} does not alter the positions of the excitation or emission peaks but leads to an enhancement in the intensities of the excitation peaks of Cu^+. The PLQY results are presented in Fig. S6, where the quantum yields of the $CaAl_2O_4$:1%Cu sample and the co-doped systems remain around 10%.

Given the intrinsic oxygen vacancy defects in the high-temperature-synthesized $CaAl_2O_4$ host,[41] as further evidenced by the high-resolution O 1s XPS spectra shown in Fig. S7, copper primarily adopts the Cu^+ state at low doping levels in the singly doped $CaAl_2O_4$. This is because the oxygen vacancies effectively compensate for Cu^+. Consequently, only Cu^+-related luminescence is observed (Fig. 2(b)). As the Cu doping concentration increases, the compensation effect of oxygen vacancies gradually becomes saturated, leading to an increase in the Cu^{2+} population. The Cu^{2+} luminescence thus appears and its intensity rises with increasing Cu concentration, reaching a maximum value at a Cu doping level of 1% (Fig. 2(f)).

The CIE 1931 chromaticity diagram and color coordinates for the $CaAl_2O_4$:1%Cu system are presented in Fig. 3, while those of the Na^+/Ln^{3+} co-doped counterparts are shown in Fig. S8, with the corresponding color coordinates detailed in Table S5 of the SI. Representative photographs of the luminescence from $CaAl_2O_4$:1%Cu under 254 nm and 365 nm excitation are provided as insets.

To understand in more detail the luminescence mechanisms of Cu^{2+} and Cu^+ in $CaAl_2O_4$, we performed electronic

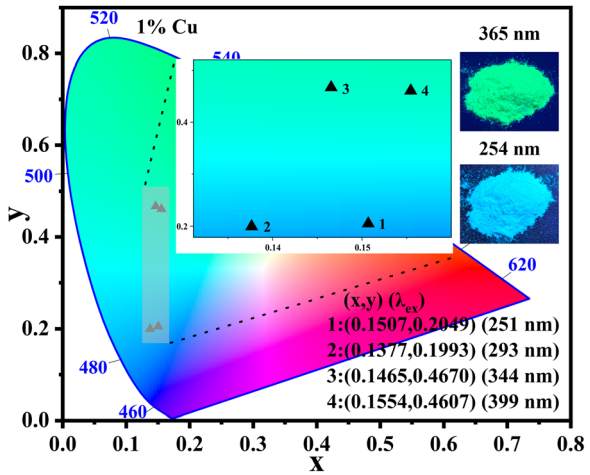


Fig. 3 CIE chromaticity diagram of $CaAl_2O_4$:1%Cu, with luminescence photographs under 254 nm and 365 nm UV excitation.

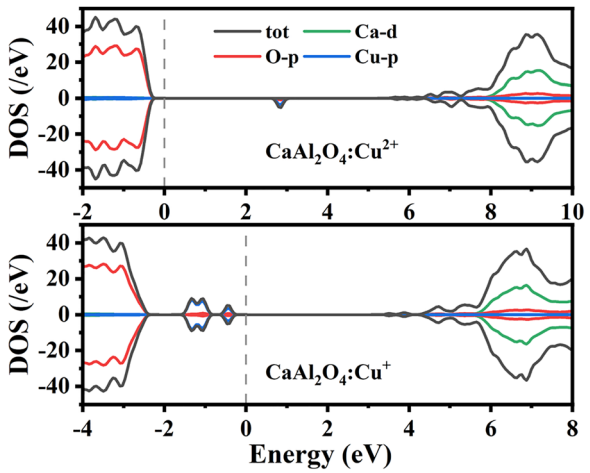


Fig. 4 The total and partial density of states (DOS and PDOS) of $CaAl_2O_4:Cu^{2+}/Cu^{+}$ with Cu incorporated on the Ca(2) site. The Fermi level is set to be 0 eV.

structure calculations of the Cu ion at its most stable Ca(2) site (Fig. 4). The results indicate that the valence band maximum (VBM) of the host lattice $CaAl_2O_4$ is dominated by O^{2-} 2p orbitals, whereas the lower conduction band region arises from hybridized contributions of O 2s/2p, Ca 3d, and Al 3s/3p orbitals, as further illustrated in the inset of Fig. S9(SI). In the case of Cu^{2+} with d^9 configuration, an unoccupied 3d orbital lies approximately 3.1 eV above the VBM. This vacant state can accept an electron from the O^{2-} 2p orbital, corresponding to an O^{2-} (2p) → Cu^{2+}(3d) CT transition. Luminescence arises from the subsequent relaxation and radiative recombination of this excited electron back to the valence band. The calculated excitation (4.346 eV, corresponding with 285 nm) and emission (2.520 eV, corresponding with 492 nm) energies agree reasonably well with the experimental spectra (4.232 eV and 2.633 eV) (Fig. 2). The two experimental CT excitation bands of Cu^{2+} are attributed to electron transfers from distinct ligand orbitals of O^{2-}, analogous to the two CT bands observed in MgO: Cu^{2+}.[37] Our calculations successfully reproduce the CT transition originating from the higher-lying O^{2-} ligand orbitals to Cu^{2+}.

For Cu^{+} with d^{10} configuration, the fully occupied 3d orbitals are situated in an energy range of 0.9–2.1 eV above the VBM. The calculated excitation energy by using the constrained occupancy approach[42–45] for promoting a 3d electron to the conduction band is 3.508 eV (353 nm), which is slightly overestimated compared to the experimental value of 3.108 eV (399 nm). Consequently, the computed emission energy for the reverse process is 2.451 eV (506 nm), closely matching the experimental value of 2.475 eV (501 nm). In summary, our electronic structure calculations provide strong theoretical support for assigning the two distinct luminescence centers in $CaAl_2O_4$ to Cu^{+} and Cu^{2+}.

3.3. Persistent luminescence performance of Cu-doped $CaAl_2O_4$

The $CaAl_2O_4:x\%Cu$ (x = 0.5–1.5) samples showed clear persistent luminescence (PersL) after 30 minutes of irradiation using a 254 nm UV source (9 W). Among the series, the composition with 1% Cu exhibited the most prolonged afterglow, lasting over 1.1 hours above the approximate visual detection threshold of 0.32 mcd m^{-2} (Fig. 5(a)). The decay of this optimal sample was accurately fitted with a biexponential function,[4,5] giving a fast lifetime component (τ_1 = 36.76 s) and a slow component (τ_2 = 276.16 s) (Fig. 5(a), inset), indicating a PersL mechanism involving a distribution of trap depths. Time-resolved PersL spectra consistently displayed a single emission band centered at 471 nm (Fig. 5(b)), which originates from the Cu^{2+} centers. The gradual fading of this blue afterglow is visually documented by the photographs in the corresponding inset. In contrast, under excitation conditions (365 nm, 9 W, 30 min), the $CaAl_2O_4$:Cu sample showed no detectable PersL, indicating that Cu^{+} ions do not exhibit persistent luminescence in this host. For co-doped samples, although Na^{+} stabilizes Cu^{2+}, it substantially shortens the afterglow duration to 760 s (Fig. S10). In contrast, no afterglow is detected in Ln^{3+}-*co*-doped samples. This is consistent with the mechanism that the persistent luminescence originates from Cu^{2+}, whereas Ln^{3+} predominantly stabilizes Cu^{+}. The TL measurement results for $CaAl_2O_4$:1%Cu are presented in Fig. S11(a). Details of the trap analysis, the Cu^{2+} persistent luminescence mechanism, and the explanation for Na^{+}-induced afterglow shortening are provided in the SI.

3.4. Thermal stability of Cu-doped $CaAl_2O_4$

The temperature-dependent excitation and emission spectra of Cu^{2+} co-doped with Na^{+} and Cu^{+} co-doped with La^{3+} in $CaAl_2O_4$, as shown in Fig. 6. The excitation spectrum monitored at 471 nm (Cu^{2+} emission) exhibits a pronounced red shift with temperature, characteristic of the O^{2-} → Cu^{2+} CT transition. In contrast, the Cu^{+}-associated excitation peaks at 344 nm and 399 nm remain highly unchanged with respect to their position across the same temperature range. As depicted in Fig. 6(a), the luminescence intensity of Cu^{2+} remains nearly constant

 This journal is © The Royal Society of Chemistry 2026

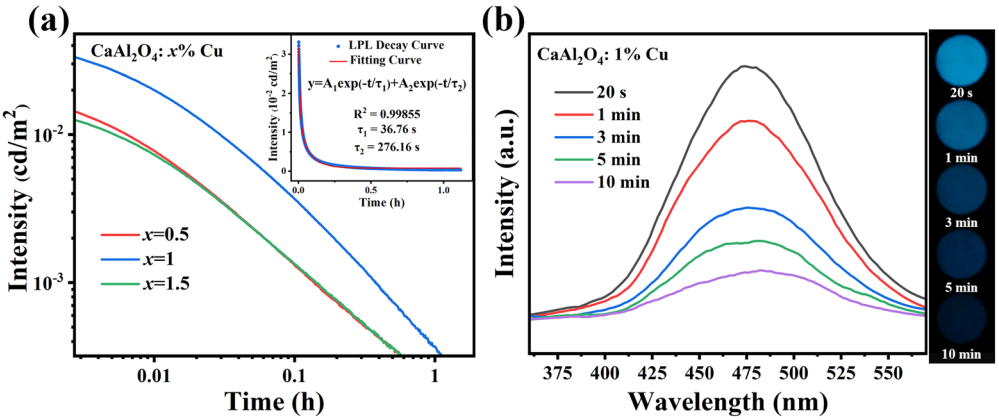


Fig. 5 (a) The PersL decay curves of $CaAl_2O_4$:*x*%Cu (*x* = 0.5–1.5) samples. The inset shows the exponentially fitting decay curves with a Cu concentration of 1%. (b) The PersL spectra of $CaAl_2O_4$:1%Cu recorded at 20 s, 1 min, 3 min, 5 min, and 10 min after removing the excitation. The inset shows photographs taken after irradiation from 20 s to 10 min.

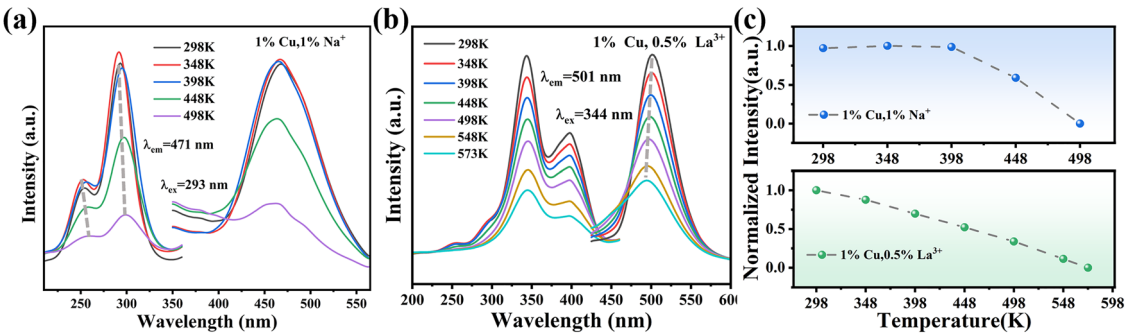


Fig. 6 Temperature-dependent excitation and emission spectra of the corresponding samples: (a) $CaAl_2O_4$:1%Cu,1%Na^+, (b) $CaAl_2O_4$:1%Cu,0.5%La^{3+}; (c) normalized integrated luminescence intensity as a function of temperature for both samples.

from 298 K to 398 K under 293 nm excitation. Beyond 398 K, a progressive decrease occurs, which can be attributed to the combined effects of thermal quenching and temperature-induced reduction of absorption of excitation radiation due to the thermal-induced peak shift. Under 344 nm excitation, the Cu^+-related emission band decreases with increasing temperature (Fig. 6(b)), yet at 573 K its emission intensity still retains 40% of the room-temperature value. The temperature-dependent integrated emission intensities of Cu^{2+} and Cu^+ are shown in Fig. 6(c), revealing distinctly different thermal quenching behaviors. Notably, the nearly constant intensity of Cu^{2+} below 398 K likely arises from the fact that, as the temperature rises, carriers trapped at intrinsic defects in the $CaAl_2O_4$ host are released and partially compensate the thermal quenching of the Cu^{2+} emission itself.

In contrast to the unchanged peak position of Cu^{2+} with increasing temperature (Fig. 6(a)), Cu^+ exhibits a blue shift of its emission spectrum as the temperature rises (Fig. 6(b)). This shift is ascribed to lattice thermal expansion, which weakens the crystal field around Cu^+ ions. The reduced crystal field strength decreases the splitting of the 3d orbitals, lowering the energy of the highest occupied 3d level and resulting in the observed blue shift. A similar trend was observed in the Tb^{3+}/Dy^{3+}-codoped systems, where the spectral behaviors of Na^+ and Ln^{3+} co-doping mirrored those of Cu^{2+} and Cu^+ luminescence, respectively (Fig. S12).

4. Optical encoding application of $CaAl_2O_4$:Cu

Based on the luminescence of multivalent Cu ions in $CaAl_2O_4$ and the selective emission control achieved through Na^+ and Ln^{3+} doping, we constructed a simple optical information encoding unit (Fig. 7). The device was fabricated by patterning equally sized square regions on a polypropylene substrate. Three samples with similar emission intensities, namely $CaAl_2O_4$:1%Cu, $CaAl_2O_4$:1%Cu,1%Na^+, and $CaAl_2O_4$:1%Cu,0.5%Dy^{3+}, were selected and placed into the designated squares. The coding rule is: black represents 0, while blue and green both represent 1. The optical encoding board demonstrates excitation-dependent information display under 254 nm and 365 nm UV illumination. After ASCII decoding, the pattern obtained under 254 nm excitation reveals the character sequence "HFUT", while that under 365 nm excitation decodes to "LOVE". As a second example, the prepared samples are filled into the pattern of the digit "88",

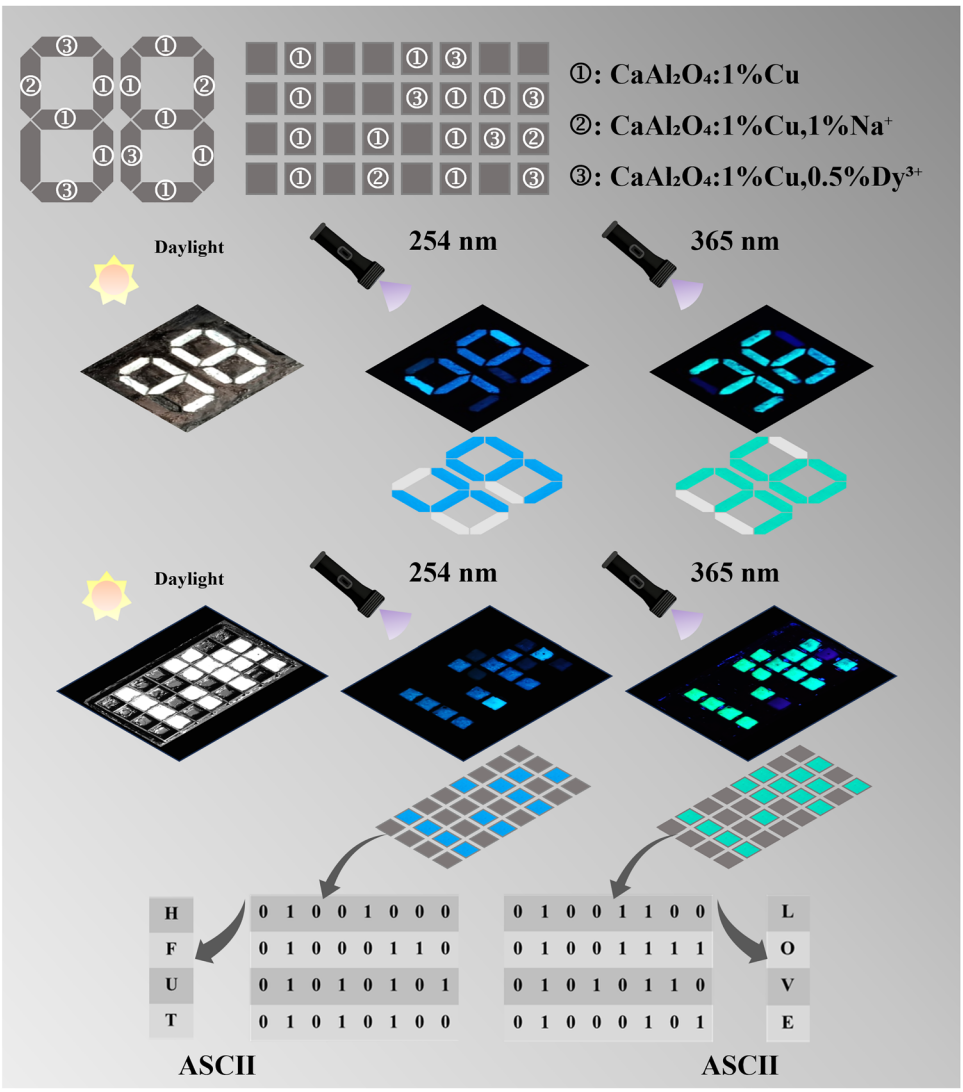


Fig. 7 Optical encoding application of luminescent materials based on $CaAl_2O_4$:1%Cu, $CaAl_2O_4$:1%Cu,1%Na^+, and $CaAl_2O_4$:1%Cu,0.5%Dy^{3+}.

the resulting display exhibits excitation-dependent numerical readouts: under 254 nm UV excitation, the number "49" is displayed, whereas under 365 nm excitation, the number "36" is revealed. This feature can be used for secure information storage and encrypted data transmission, broadening the applications of multimodal luminescent materials in optical storage and encryption.

5. Conclusion

In conclusion, we have investigated the valence state and luminescence properties of Cu in $CaAl_2O_4$ by means of Na^+ and Ln^{3+} co-doping. We demonstrate that Na^+ co-doping stabilizes Cu^{2+}, resulting in a blue emission at 471 nm, whereas trivalent lanthanide co-doping promotes Cu^+, yielding a green emission at 501 nm. This targeted valence control enables the unambiguous assignment of each broadband emission to a specific copper oxidation state. This resolves the persistent challenge of spectrally distinguishing Cu^+ and Cu^{2+} emissions in phosphors for decades. The direct correlation between co-dopant, valence state, and emission color allows for selective excitation and switching between these two distinct luminescence centers. This work explores the application potential of Cu^+/Cu^{2+} dual-valence luminescence in areas such as anti-counterfeiting and provides the feasibility for the design and development of novel copper-activated luminescent materials.

Conflicts of interest

There are no conflicts to declare.

Data availability

All of the data that support the findings in this study are available within the article and its supplementary information (SI).

This journal is © The Royal Society of Chemistry 2026

Supplementary information: DFT calculation parameters, XRD patterns of samples, Cu Auger lines, quantum efficiency data, persistent luminescence mechanism analysis (PDF). See DOI: https://doi.org/10.1039/d6tc01463a.

Acknowledgements

This work is supported by the National Natural Science Foundation of China (Grant 52372143), the Industrial Innovation Guidance Fund of Tongcheng City & Hefei University of Technology (JZ2022YDZJ0083), and the Fundamental Research Funds for the Central Universities (PA2022GDGP0029, PA2023GDGP0042). The computation is completed on the HPC Platform of Hefei University of Technology. We thank the staff members of the Electron Spin Resonance System(https://cstr.cn/31125.02.SHMFF.ESR) at the Steady High Magnetic Field Facility, Chinese Academy of Sciences (https://cstr.cn/31125.02.SHMFF), for providing technical support and assistance in data collection and analysis.

References

1 A. Wang, A. Huang and H. Zhao, *et al.*, Optical storage and encryption via efficient reversible luminescence modulation based on copper-doped borate glass, *Chem. Eng. J.*, 2024, **487**, 150648.
2 H. Guo, R. Wei and X. Liu, Tunable white luminescence and energy transfer in $(Cu^{+})_2$, Eu^{3+} codoped sodium silicate glasses, *Opt. Lett.*, 2012, **37**(10), 1670.
3 K. Lei, J. Feng and Y. Sun, *et al.*, Structure and luminescence properties of Cu^{+} doped glasses prepared by ion exchange, *J. Non-Cryst. Solids*, 2023, **605**, 122158.
4 L. Wang, C. Wang and Y. Chen, *et al.*, Red-Emitting $SrGa_2O_4$:Cu^{2+} phosphor with super-long persistent luminescence, *Chem. Mater.*, 2022, **34**(22), 10068–10076.
5 Z. Li, Y. Ding and S. Zhang, *et al.*, Temperature-dependent trap engineering in gallate long afterglow phosphor for advanced information encryption and anti-counterfeiting, *Nano Mater. Sci.*, 2025, DOI: 10.1016/j.nanoms.2025.10.016.
6 L. Wang, N. Zhao and C. Zhu, *et al.*, Tunable visible emission and persistent luminescence of $BaGa_2O_4$:Cu^{2+}, *Chem. Eng. J.*, 2024, **483**, 149361.
7 L. Wang, B. Xiao and C. Wang, *et al.*, Ultra-long green persistent luminescence from Cu^{2+} in $Ba_{0.4}Sr_{1.6}Ga_4O_8$, *Chem. Mater.*, 2026, **38**(11), 5481–5488.
8 X. Peng, R. Li and Y. Zhang, *et al.*, Cation engineering enables visible tunable tricolor long persistent luminescence in Cu^{2+}-activated phosphors for advanced information encryption, *Chem. Eng. J.*, 2025, **523**, 168396.
9 L. Wang, C. Wang, Y. Chen, B. Qu, C. Zhu, P. Dai, Y. Jiang and L. Chen, A type of Cu ion-doped gallate-based green emission persistent luminescence material and its preparation method, CN202211207418.0, 2024.
10 T. Zhang, H. Yuan and P. Wu, *et al.*, Long persistent luminescence in Cu^{2+}-doped $SrGa_2Ge_2O_8$ for information storage and encryption, *Inorg. Chem.*, 2025, **64**(4), 2072–2079.
11 W. M. Mulwa, B. F. Dejene and M. O. Onani, *et al.*, Effect of Cu^{2+} doping on the structural, electronic, and optical properties of $ZnAl_2O_4$: a combined experimental and DFT+U study, *J. Lumin.*, 2017, **184**, 7–16.
12 V. M. Maphiri, M. R. Mhlongo and T. T. Hlatshwayo, *et al.*, Citrate sol-gel synthesis of $BaAl_2O_4$:x% Cu^{2+} ($0 \leq x \leq 1$) nano-phosphors: structural, morphological and photoluminescence properties, *Opt. Mater.*, 2020, **109**, 110244.
13 K. E. Knowles, H. D. Nelson and T. B. Kilburn, *et al.*, Singlet-triplet splittings in the luminescent excited states of colloidal Cu^{+}: CdSe, Cu^{+}: InP, and $CuInS_2$ nanocrystals: charge-transfer configurations and self-trapped excitons, *J. Am. Chem. Soc.*, 2015, **137**(40), 13138–13147.
14 S. K. Sharma, S. S. Pitale and M. Manzar Malik, *et al.*, Spectral and defect analysis of Cu-doped combustion synthesized new $SrAl_4O_7$ phosphor, *J. Lumin.*, 2010, **130**(2), 240–248.
15 S. Wang, R. Liu and J. Li, *et al.*, Blue long afterglow and ultra broadband Vis-NIR emission from all-inorganic copper-doped silver halide single crystals, *Angew. Chem., Int. Ed.*, 2024, **63**(25), e202403927.
16 J. Wu, X. Zhao and W. Wang, *et al.*, Aqueous synthesis of stable Pb(OH)Br: Cu red phosphor with DFT insights into its luminescence mechanism, *Opt. Mater.*, 2025, **167**, 117319.
17 Y. Zorenko, T. Voznyak and R. Turchak, Luminescence of Cu^{+} and Cu^{2+} ions in CsBr crystals, *Acta Phys. Pol., A*, 2010, **117**(1), 199–202.
18 D. J. Lee, Y. S. Lee and H. J. Noh, Multicolor tunable emission induced by Cu ion doping of perovskite zirconate, *J. Lumin.*, 2016, **169**, 128–131.
19 A. Abulai, T. Yusufu and A. Shafuti, *et al.*, Luminescence properties of thenardite activated with Cu, *Spectrosc. Spectral Anal.*, 2011, **31**(5), 1197–1199.
20 V. Hayez, A. Franquet and A. Hubin, *et al.*, XPS study of the atmospheric corrosion of copper alloys of archaeological interest, *Surf. Interface Anal.*, 2004, **36**(8), 876–879.
21 S. Poulston, P. M. Parlett and P. Stone, *et al.*, Surface oxidation and reduction of CuO and Cu_2O studied using XPS and XAES, *Surf. Interface Anal.*, 1996, **24**(12), 811–820.
22 C. C. Ding, Y. Q. Li and Y. J. Sun, *et al.*, Investigation of the defect Cu^{2+} centers in the paddle wheel MOF: Defective structures, EPR spectra, and H_2O adsorption, *Inorg. Chem.*, 2025, **64**(28), 14063–14072.
23 O. Balitskii, W. Kagabo and P. V. Radovanovic, Composition-dependent Eu^{3+} emission in colloidal lead-free halide perovskite nanocrystals: Potential for anti-counterfeiting applications, *Rare Met.*, 2025, **44**(9), 6594–6601.
24 J. Ma, Y. Li and W. Hu, *et al.*, A terbium activated multicolour photoluminescent phosphor for luminescent anticounterfeiting, *J. Rare Earths*, 2020, **38**(10), 1039–1043.
25 X. Zhou, L. Ning and J. Qiao, *et al.*, Interplay of defect levels and rare earth emission centers in multimode luminescent phosphors, *Nat. Commun.*, 2022, **13**(1), 7589.
26 O. Balitskii, W. Kagabo and P. V. Radovanovic, Selective excitation of lanthanide co-dopants in colloidal lead-free

halide perovskite nanocrystals as a multilevel anti-counterfeiting approach, *Nanomaterials*, 2025, **15**(24), 1838.
27 T. Jiang, Y. Zhu and J. Zhang, *et al.*, Multistimuli-responsive display materials to encrypt differentiated information in bright and dark fields, *Adv. Funct. Mater.*, 2019, **29**(51), 1906068.
28 X. Xu, S. Xu and B. Man, *et al.*, Defect-engineered $Ca_5Ga_6O_{14}$:Ti^{4+}, Sm^{3+} multi-stimuli-responsive luminescent nanophosphor for macro-micro anti-counterfeiting and multilevel encoding, *Adv. Funct. Mater.*, 2025, **36**(9), e17527.
29 J. Zhou and Z. Xia, Luminescence color tuning of Ce^{3+}, Tb^{3+}, and Eu^{3+} codoped and tri-doped $BaY_2Si_3O_{10}$ phosphors *via* energy transfer, *J. Mater. Chem. C*, 2015, **3**(29), 7552–7560.
30 W. Hörkner and Hk Müller-Buschbaum, Zur Kristallstruktur von $CaAl_2O_4$, *J. Inorg. Nucl. Chem.*, 1976, **38**(5), 983–984.
31 K. A. Gedekar, S. P. Wankhede and S. V. Moharil, Synthesis and comparative study of Ce^{3+} ion in calcium aluminates, *J. Sol-Gel Sci. Technol.*, 2017, **82**(2), 344–351.
32 K. A. Gedekar, S. P. Wankhede and S. V. Moharil, *et al.*, d-f luminescence of Ce^{3+} and Eu^{2+} ions in $BaAl_2O_4$, $SrAl_2O_4$, and $CaAl_2O_4$ phosphors, *J. Adv. Ceram.*, 2017, **6**(4), 341–350.
33 J. A. Torres-Ochoa, D. Cabrera-German and O. Cortazar-Martínez, *et al.*, Peak-fitting of Cu 2p photoemission spectra in Cu^0, Cu^{1+}, and Cu^{2+} oxides: A method for discriminating Cu^0 from Cu^{1+}, *Appl. Surf. Sci.*, 2023, **622**, 156960.
34 Z. Li, Y. Xin and Z. Zhang, *et al.*, Rational design of binder-free noble metal/metal oxide arrays with nanocauliflower structure for wide linear range nonenzymatic glucose detection, *Sci. Rep.*, 2015, **5**(1), 10617.
35 G. Li, T. Long and Y. Song, *et al.*, Preparation and luminescent properties of $CaAl_2O_4$:Eu^{3+}, R^+ (R = Li, Na, K) phosphors, *J. Rare Earths*, 2010, **28**(1), 22–25.
36 S. Vishwakarma, O. S. Tiwari and D. Banerjee, *et al.*, Multienzyme (3-in-1)-mimicking a single nucleobase-derived bionanozyme for versatile environmental and biomedical applications, *Adv. Healthcare Mater.*, 2025, **14**(24), 2501435.
37 J. L. Pascual, B. Savoini and R. González, Electronic absorption spectra of Cu^{2+} in MgO: ab initio theory and experiment, *Phys. Rev. B: Condens. Matter Mater. Phys.*, 2004, **70**(4), 045109.
38 N. Y. Nobuhiko Yamashita, Photoluminescence properties of Cu^+ centers in MgS, CaS, SrS, and BrS, *Jpn. J. Appl. Phys.*, 1991, **30**(12R), 3335.
39 D. Jia, X.-J. Wang and W. M. Yen, Electron traps in Tb^{3+}-doped $CaAl_2O_4$, *Chem. Phys. Lett.*, 2002, **363**(3), 241–244.
40 B.-G. Zhai, M. M. Chen and Y. M. Huang, Photoluminescence and afterglow of Dy^{3+} doped $CaAl_2O_4$ derived via sol-gel combustion, *RSC Adv.*, 2022, **12**(49), 31757–31768.
41 T. Aitasalo, J. Hölsä and H. Jungner, *et al.*, Thermoluminescence study of persistent luminescence materials: Eu^{2+}- and R^{3+}-doped calcium aluminates, $CaAl_2O_4$:Eu^{2+}, R^{3+}, *J. Phys. Chem. B*, 2006, **110**(10), 4589–4598.
42 Y. Jia, S. Poncé and A. Miglio, *et al.*, Assessment of first-principles and semiempirical methodologies for absorption and emission energies of Ce^{3+}-doped luminescent materials, *Adv. Opt. Mater.*, 2017, **5**(7), 1600997.
43 J. Cai, W. Jing and J. Cheng, *et al.*, First-principles calculations of photoluminescence and defect states of Ce^{3+}-doped $(Ca/Sr)_2B_5O_9Cl$, *Phys. Rev. B*, 2019, **99**(12), 125107.
44 Y. Jia, A. Miglio and S. Poncé, *et al.*, First-principles study of Ce^{3+}-doped lanthanum silicate nitride phosphors: Neutral excitation, Stokes shift, and luminescent center identification, *Phys. Rev. B*, 2016, **93**(15), 155111.
45 A. Canning, A. Chaudhry and R. Boutchko, *et al.*, First-principles study of luminescence in Ce-doped inorganic scintillators, *Phys. Rev. B: Condens. Matter Mater. Phys.*, 2011, **83**(12), 125115.

 This journal is © The Royal Society of Chemistry 2026